Acta Crystallographica Section A
**Foundations of Crystallography**
ISSN 0108-7673

Received 18 April 2000
Accepted 24 July 2000

*Dedicated to Professor Karl F. Fischer on the occasion of his 75th birthday*



# Topological analyses of cuprite, $Cu_2O$, using high-energy synchrotron-radiation data

**Thomas Lippmann* and Jochen R. Schneider**

Hamburger Synchrotronstrahlungslabor HASYLAB at Deutsches Elektronen-Synchrotron DESY, Notkestrasse 85, D-22603 Hamburg, Germany. Correspondence e-mail: thomas.lippmann@desy.de

Topological analyses were performed on room-temperature and low-temperature high-energy synchrotron-radiation data from cuprite, $Cu_2O$, using both single-exponential and analytical functions in the multipole model. Differences between the refinements of the data sets turned out to be small and the data were found to be well suited for the analyses and for evaluations of further properties, *e.g.* the electrostatic potential and the Laplacian. The ionic character of the the copper–oxygen bond was impressively underlined by the results. On the 'empty' tetrahedral sites, minima of the charge density were always found.

## 1. Introduction

Recently, we presented structure refinement results of cuprite, $Cu_2O$, using high-energy synchrotron-radiation data (Lippmann & Schneider, 2000, referred to as LS hereinafter). The investigations were intended as a test for the usefulness of the available hard- and software at the HASYLAB high-energy beamline BW5 (Bouchard *et al.*, 1997) for charge-density studies. The data quality turned out to be very well suited for multipole refinements. Additionally, we could show that it was possible to extract an extinction-free data set prior to the refinement if intensities of strong low-order reflections from multiple-energy data measured in the regime 75 to 150 keV were used.

We decided to perform topological analyses on both extinction-affected and extinction-free data in order to test the potential of high-energy synchrotron data for quantitative evaluations and to work out similarities and differences of the two data sets. Following the fundamental work of Bader (1990) on the topological analysis of charge-density distributions, numerous studies have meanwhile been published, which include both applications and further developments of the method. Most of the applications deal with comparisons between theoretical and experimental results (Gatti *et al.*, 1992) or investigations of a series of exclusive structures or data sets (Espinosa *et al.*, 1998). Developments are, for instance, focused on methods for the derivation of more information from the analyses. For example, Abramov (1997) proposed a functional for a relation between topological parameters at the bond critical point and the kinetic energy. Further work deals with practical computing algorithms for the graphical mapping and analysis of the density, the gradient vector field and the Laplacian *etc.* (Souhassou & Blessing, 1999).

In addition to the analysis of the total charge density itself, valuable information is also provided by analysing quantities derived from the density, especially the electrostatic moments (Spackman, 1992), the potential (Politzer & Truhlar, 1981) and the Laplacian (Flensburg *et al.*, 1995; Flaig *et al.*, 1998).

Selecting cuprite as test structure for our investigations was not arbitrary since it had earlier been examined using conventional X-rays (Lewis *et al.*, 1982; Restori & Schwarzenbach, 1986) and 'low-energy' synchrotron radiation (Kirfel & Eichhorn, 1990), which made comparisons easily possible. Moreover, a sample from the same origin as used in the latter experiment was available and the same data-analysis software was applied.

The chemical bonding of copper and oxygen has recently gained much interest owing to its importance in high-$T_c$ superconductors (Humphreys, 1999). Hence, the results presented here can be regarded as a preliminary stage to a forthcoming investigation of superconductor structures.

15 years ago, Nagel (1985) and Marksteiner *et al.* (1986) published theoretical calculations of the charge density of cuprite. They found that the charge densities at copper and oxygen are not spherically symmetric. Additionally, it was assumed that the Cu—O distance of 1.85 Å is considerably smaller than the sum of the ionic radii, which leads to the hypothesis of a covalent-bonding fraction. However, recently, Wang & Schwarz (2000) pointed out that the sum of the ionic radii fits quite well the separation of the ions in cuprite. Moreover, the experimentally observed charge depletion in the region between the ions by Kirfel & Eichhorn (1990) and LS is in contrast to the naive assumption of covalency, see *e.g.* Schwarz *et al.* (1986, 1989) and Irle *et al.* (1992). Thus, it seems worthwhile to perform a topological analysis in order to determine the properties at the bond critical points quantitatively.

**Table 1**
Refined data sets; $N$ is the number of unique reflections.

| Data set | Explanation | $N$ |
|---|---|---|
| CUHE | Room temperature data | 152 |
| CUEC | 9 extinction-corrected reflections + 143 extinction-free reflections of CUHE | 152 |
| CULT | 20 K data | 150 |

**Table 2**
Number of reflections contributing to the different parity groups.

| Parity group | 20 K data | 300 K data |
|---|---|---|
| *ooo* | 34 | 32 |
| *eee* | 40 | 46 |
| *ooe* | 66 | 55 |
| *eeo* | 10 | 19 |
| $\sum$ | 150 | 152 |

**Table 3**
Refinement models.

| Model | Function(s) |
|---|---|
| EXP | Single exponentials |
| AN1 | Analytical functions for Cu and O |
| AN2 | Analytical functions for $Cu^+$ and O (three form-factor shells) |
| AN3 | Analytical functions for $Cu^+$ and O (four form-factor shells) |

Since cuprite has a hardness of 4 and a Debye temperature of only 184 K, both thermal diffuse scattering and the $U^{ij}$ of the Debye–Waller factors are large compared with those of well known standard structures like corundum or silicon. In order to check the reliability of the refinement parameters obtained from the ambient temperature measurements, they are compared to the results of a low-temperature experiment.

The paper is organized as follows: first, the refinement results of our high-energy synchrotron-radiation data sets are briefly summarized and the results of the new low-temperature data refinement are presented. Then, the critical points of the charge-density distributions are presented and analyzed. In addition, space partitioning was performed, and further properties like the electrostatic potential and the Laplacian of the density are presented. Additionally, the electric field gradient was investigated. The presentation of the analyses is completed by a comparison of the charge density on the 'empty' tetrahedral sites with the results recently published by Zuo *et al.* (1999). Finally, our results are summarized and conclusions are made.

## 2. Data and refinements

The room-temperature (CUHE) and the extinction-corrected (CUEC, Table 1) data sets have already been presented in LS. Additionally, a low-temperature experiment at 20 K was performed on the same sample and the data set (CULT) consisted of 150 unique reflections up to $\sin\theta/\lambda = 1.2$ Å$^{-1}$. All data were measured using 100 keV synchrotron radiation at the HASYLAB high-energy beamline BW5. The data reduction was carried out as described in LS.

High- and low-temperature data sets differ in two features. On the one hand, many weak high-order reflections, which are insignificant at room temperature, have significant intensities at low temperatures. On the other hand, the very weak so-called 'forbidden' reflections (reflection indices *eeo*, $e$ = even, $o$ = odd) are mainly due to anisotropic thermal vibrations and, hence, most of them are insignificant at low temperatures. Table 2 presents the number of reflections contributing to the four parity groups for the different data sets.

Multipole refinements were performed using four different models, which are based on different orbital functions (Table 3).

(*a*) EXP: analytical Hartree–Fock wave functions (Clementi & Roetti, 1974), which had been expanded in terms of Slater-type basis functions and included as fixed linear combinations in both *XD* (Koritsanszky *et al.*, 1995) and *VALRAY* (Stewart & Spackman, 1983), were applied for the core density. For the valence electrons and higher multipoles, single Slater-type exponentials were used.

(*b*) AN1: the fixed linear combinations of the expanded analytical neutral-atom Hartree–Fock wave functions were used for all monopoles and multipoles.

(*c*) and (*d*) AN2 and AN3: compared with AN1, the Cu neutral-atom functions were replaced by two types of analytical functions for $Cu^+$ with different contributions to the monopole shells. The $Cu^+$ functions were calculated by R. F. Stewart.

Model AN2 is based on three form-factor shells assuming 2 electrons in the core, 8 electrons in the inner and 18 electrons in the outer valence shell. Model AN3 follows a chemical-type partitioning, which used four monopole form-factor shells including 2, 8, 8 and 10 electrons, respectively. The overlap of the third and fourth shells was 0.964, which reflects the similar compactness of the 3*d* with the outer *s* and *p* self-orbital products (Stewart, 1999). In the refinement using AN3 functions, the first- and second-shell electrons were considered as the core.

Refinements using models EXP and AN1 were started with neutral atoms as promolecule, and AN2 and AN3 with $Cu^+$ and $O^{2-}$, respectively. The strategy was based on a start cycle using the independent-atom model (IAM) in order to find start parameters for the anisotropic thermal displacement factors (TDF) and the extinction, and subsequent cycles including at first only the population coefficients of the higher multipoles, then the radial parameters and finally also the valence monopole parameters. During the multipole refinement, the IAM was re-refined several times in order to check the TDFs and to stabilize the procedure. The TDFs varied only a few $\sigma$ in all cases. In the last cycle, the significantly changed parameters were refined altogether in order to find the absolute minimum of the fit. In the case of $\kappa'$ refinements, however, these had to be fixed in the last cycles. Table 4 summarizes the $R(F)$'s, $R_w(F)$'s and the goodnesses of fit as derived from *VALRAY* refinements. All refinements converged yielding agreement and weighted agreement factors below 1%.

**Table 4**
Refinement results: $R(F)$ / $R_w(F)$ / GoF; source: *VALRAY*.

| Data | EXP | AN1 | AN2 | AN3 |
|---|---|---|---|---|
| CUHE | 0.0045 / 0.0082 / 1.07 | 0.0068 / 0.0091 / 1.19 | 0.0067 / 0.0091 / 1.19 | 0.0077 / 0.0094 / 1.23 |
| CUEC | 0.0085 / 0.0089 / 1.17 | 0.0087 / 0.0088 / 1.16 | 0.0086 / 0.0090 / 1.18 | 0.0093 / 0.0092 / 1.21 |
| CULT | 0.0059 / 0.0082 / 1.16 | 0.0054 / 0.0085 / 1.19 | 0.0059 / 0.0090 / 1.26 | 0.0057 / 0.0090 / 1.27 |

The weighted agreement factors vary between 0.0082 and 0.0094 and showed no significant differences comparing the data sets with each other. The same holds for a comparison of the different models. All goodnesses of fit were close to one (1.11–1.27), but a closer look reveals that the EXP refinements were marginally better than the refinements using analytical functions. This trend is emphasized by a comparison of the residual indices $R(F)$, *e.g.* using the CUHE data 0.0049 for the EXP model and 0.0067–0.0077 for the analytical function models. Here, the use of AN1 and AN2 also yields an improved fit compared with model AN3. Further tests showed that only the choice of the valence monopole function is responsible for the differences.

Additionally, improved agreement indices are found for the CUHE and CULT data sets compared with CUEC. This behaviour is due to a deterioration of the statistical accuracy of the data by the extinction correction, as has already been mentioned in LS.

In order to cross-check the results, all refinements were carried out using both *VALRAY* (Stewart & Spackman, 1983) and *XD* (Koritsanszky *et al.*, 1995), which differ in refining the radial functions of the single exponentials. Using *XD*, the parameter $\kappa'$ in

$$R_l(\kappa' r) = \frac{\zeta_l^{n(l)+2}}{[n(l)+3]!}(\kappa' r)^{n(l)} \exp(-\zeta_l \kappa' r) \quad (1)$$

was refined, whereas in *VALRAY* the refinements are based on the fit of $\alpha$ in

$$R_l(r) = \frac{\alpha_l^{n(l)+3}}{[n(l)+2]!}(r)^{n(l)} \exp(-\alpha_l r). \quad (2)$$

The refinement-program differences are shown in Table 5 for the data set CUHE and the model EXP. The differences for $R(F)$, $R_w(F)$ and the GoF were always found to be below 2% and for the TDFs below 3%, respectively. Note that, owing to different normalization factors, the population parameters cannot be compared. A second check was performed using *XD* and the analytical functions provided by *VALRAY* and *vice versa*. Again, no significant differences occurred. Hence, we concluded that the refinement results were not dependent on the refinement programs but only on the data and the models.

Fig. 1 shows the total charge density in the copper–oxygen plane derived from the three data sets using model EXP. Total density maps are presented here because these data were used for the critical-point determinations and analyses. Differences between the maps are only visible in the low-density regions and the differences are small. Error maps were calculated using the variance–covariance matrix $\varepsilon$, *i.e.* the variance in property $A$ derived from $N_v$ parameters $P_i$ is calculated by

$$\sigma^2(A) = S^2 \sum_{i,j}^{N_v} \left(\frac{dA}{dP_i}\right) \varepsilon_{ij} \left(\frac{dA}{dP_j}\right), \quad (3)$$

where $S$ is the goodness of fit (Cruickshank & Robertson, 1953; Koritsanszky *et al.*, 1995). The corresponding error maps show various features, but on a scale that is several orders of magnitude below the scale of the density maps. This is illustrated in detail in Figs. 2(*a*)–(*f*), where sections of the maps are presented. For example, the maximum error in Fig. 2(*d*) is

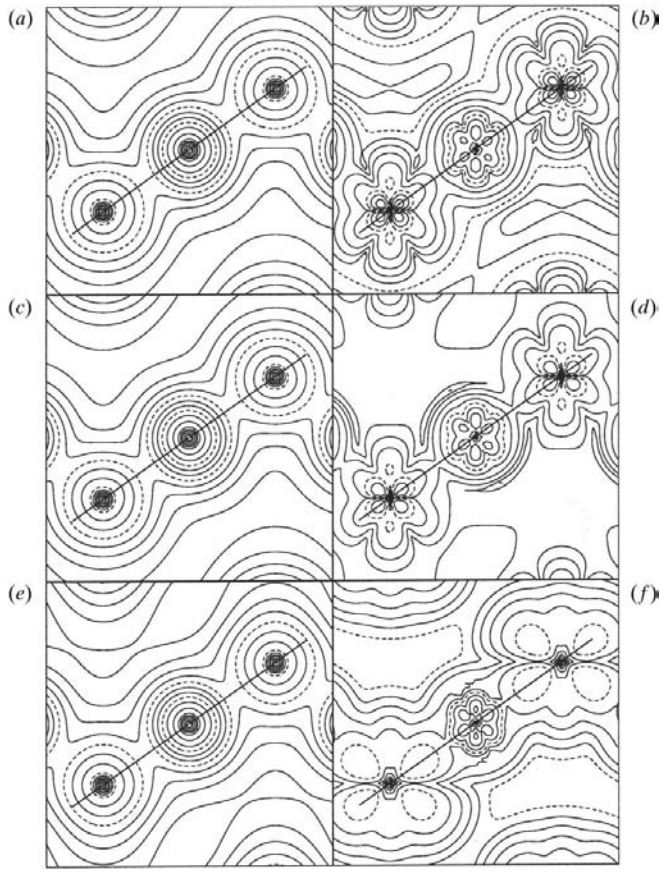


**Figure 1**
5 × 5 Å maps of the total charge density in the (110) plane derived from (*a*) CUHE–EXP, (*c*) CUEC–EXP and (*e*) CULT–EXP. Contour lines on a geometrical scale, starting at 0.15 e Å$^{-3}$, line $n$ at 0.15 × 2$^n$. Lines at 1.2 and ∼10 e Å$^{-3}$ are dashed. Centre at 0,0,0. Corresponding error maps derived from (*b*) CUHE–EXP, (*d*) CUEC–EXP and (*f*) CULT–EXP. Contours starting at 0.005 e Å$^{-3}$, line $n$ at 0.005 × 1.5$^n$. Dashed lines at 0.011 and 0.086 e Å$^{-3}$. The densities along the straight lines are shown in Fig. 2. Source: *VALRAY*.

**Table 5**
Multipole refinement results of CUHE–EXP.

| | Parameter | *VALRAY* | *XD* |
|---|---|---|---|
| Cu | $U^{11}$ | 1935 (1) | 1932 (3) |
| | $U^{12}$ | −85.7 (5) | −86.7 (11) |
| | $\alpha_0$ | 5.9 (5) | |
| | $\alpha_2$ | 5.27 (6) | |
| | $\alpha_4$ | 6.6 (2) | |
| | $\kappa'$ | | 2.44 (1) |
| | $Y_{20}$ | −0.63 (2) | −0.10 (1) |
| | $Y_c$ | 0.23 (4) | 0.09 (2) |
| O | $U_{iso}$ | 1878 (4) | 1890 (7) |
| | $\alpha_0$ | 3.7 (1) | |
| | $\alpha_3$ | 6.9 (6) | |
| | $\alpha_4$ | 3.8 (5) | |
| | $\kappa$ | | 0.998 (3) |
| | $\kappa_l$ | | 1.67 (2) |
| | $Y_{32-}$ | −0.13 (3) | −0.010 (3) |
| | $Y_c$ | −0.8 (2) | −0.017 (6) |
| | CT | 0.57 (3) | 0.62 (4) |
| | $R(F)$ | 0.0045 | 0.0046 |
| | $R_w(F)$ | 0.0082 | 0.0083 |
| | GoF | 1.07 | 1.08 |

Explanation of symbols used above and in the text.

| Parameter | Explanation |
|---|---|
| $U^{ij}$ | $\times 10^5$ Å$^2$ |
| $\alpha_i, \kappa'$ | Radial parameters |
| $Y_c$ | Cubic hexadecapole |
| CT | Formal charge transfer from Cu towards O |

0.23 e Å$^{-3}$ and has to be compared with a density of about 50 e Å$^{-3}$ in Fig. 2(*c*). A comparison of the maximum errors of the different data sets shows similarities between CUHE and CUEC, *i.e.* the maxima near the copper and the oxygen nuclei are approximately equal in height. The low-temperature data, however, yield much smaller errors near the oxygen nuclei. The reason is obviously the different consistency of the data sets. The CULT data have a larger percentage of weak high-order *ooe* ('oxygen') reflections (see Table 2), which leads to a more precise determination of the density near oxygen.

## 3. Examination of the critical points

Bader's topological analysis is now well established as a powerful tool for a quantitative examination and description of charge densities and chemical bonds, and the algorithms have been coded and implemented in structure refinement and analysis computer-program packages. Both *VALRAY* and *XD* allow for the analysis of the gradient vector field of a three-dimensional charge-density distribution in order to find the 'critical points', where the gradient vanishes. By diagonalization of the Hessian matrix, which consists of the second derivatives of the charge density, *i.e.* the matrix elements are $\partial^2\rho/\partial x_i \partial x_j$, the eigenvalues can be found, and these principal curvatures are used to characterize the critical points and to divide them up into four groups: (3,−3) peaks or local maxima, where all second derivatives are negative; (3,−1) passes or saddle points, where two are negative and one is positive; (3,+1) pales or ring citical points, where one is negative and two are positive; and (3,+3) pits or local minima, where all second derivatives are positive (Johnson & Burnett, 1996).

At first, all unique critical points in the cuprite unit cell were determined. In both computer programs, the search of the critical points is based on algorithms, which start on given points in the gradient field and trace the gradient vector back until a critical point is reached. Using *XD*, the systematic search was carried out in a polar coordinate system, *i.e.* on shells around 0.5,0.5,0.5. The shell radius was varied in steps of 0.1 Å and the maximum radius was $3^{1/2}a_0/2$. Using *VALRAY*, a cubic grid (edge lengths $a_0$) was used as start value. A raster of 0.1 Å was chosen, starting at fractional coordinate 0,0,0 and ending at 1.0,1.0,1.0.

Since both rasters were chosen with rather narrow distances, many critical points were found several times, and these duplicates had to be sorted out. This procedure reduced

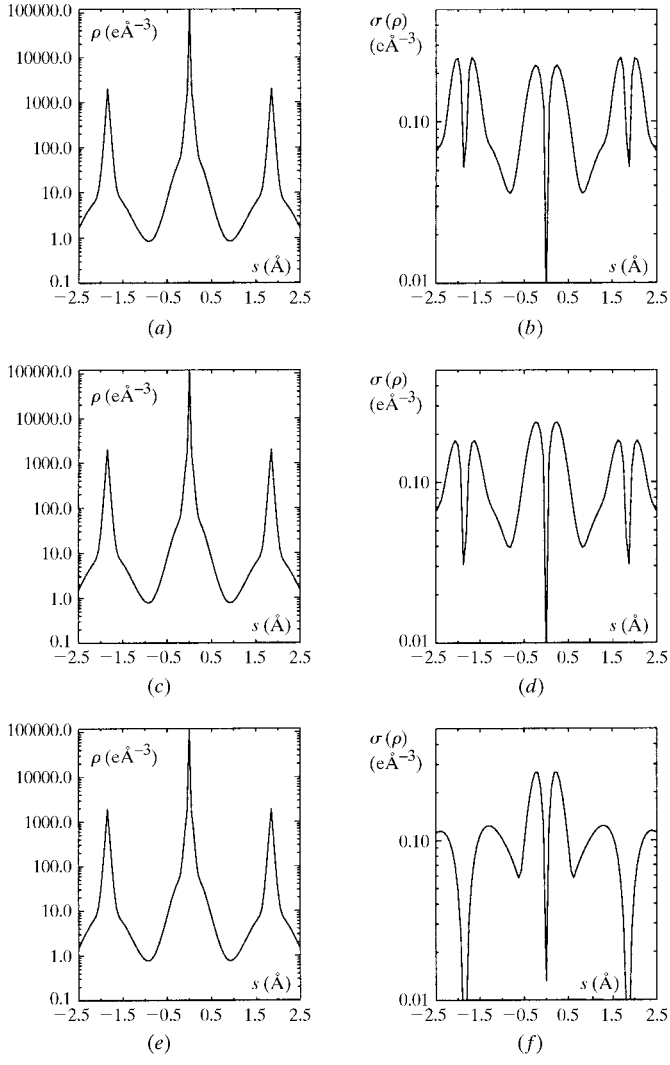


**Figure 2**
Charge density along the lines indicated in Fig. 1. (*a*) CUHE–EXP, (*c*) CUEC–EXP and (*e*) CULT–EXP, and corresponding errors (*b*), (*d*) and (*f*).

**Table 6**
Unique critical points in the unit cell of cuprite found by *VALRAY*; data: CUHE–EXP.

The maxima at the nuclei are omitted. The table shows the fractional coordinates, the critical point type, the charge density $\rho$ (e Å$^{-3}$) at the points, the Laplacian $\nabla^2\rho$ (e Å$^{-5}$) and the eigenvalues $\lambda_i$ of the Hessian; source: *VALRAY*.

| No. | $x$ | $y$ | $z$ | Type | $\rho$ | $\nabla^2\rho$ | $\lambda_1$ | $\lambda_2$ | $\lambda_3$ |
|---|---|---|---|---|---|---|---|---|---|
| 1 | 0.1227 (2) | 0.1227 (2) | 0.1227 (2) | (3,−1) | 0.816 (2) | 14.872 (38) | −4.106 (29) | −4.106 (29) | 23.084 (36) |
| 2 | 0.75 | 0.25 | 0.0 | (3,−1) | 0.092† | 0.607† | −0.119† | −0.114† | 0.838† |
| 3 | 0.6746 (1) | 0.1548 (1) | 0.1548 (1) | (3,+1) | 0.073† | 0.405† | −0.059† | 0.139† | 0.325† |
| 4 | 0.75 | 0.25 | 0.25 | (3,+3) | 0.068† | 0.325† | 0.090† | 0.090† | 0.145† |
| 5 | 0.5 | 0.0 | 0.0 | (3,+3) | 0.058† | 0.379 (1) | 0.031† | 0.031† | 0.317 (1) |

† E.s.d. less than 0.001.

**Table 7**
First rows: location of the bond critical point (fractional coordinates $x = y = z$); second rows: charge density $\rho$ (e Å$^{-3}$) at these points; source: *VALRAY*.

| Data | EXP | AN1 | AN2 | AN3 |
|---|---|---|---|---|
| CUHE | 0.1227 (2) | 0.1248 (25) | 0.1241 (10) | 0.1248 (11) |
| | 0.816 (2) | 0.793 (13) | 0.766 (12) | 0.789 (14) |
| CUEC | 0.1247 (2) | 0.1250 (10) | 0.1267 (10) | 0.1263 (11) |
| | 0.773 (2) | 0.756 (9) | 0.761 (8) | 0.749 (9) |
| CULT | 0.1256 (8) | 0.1261 (38) | 0.1262 (13) | 0.1266 (14) |
| | 0.758 (9) | 0.696 (20) | 0.673 (16) | 0.685 (17) |

the number of points to 60: 6 maxima, 20 bond points, 24 ring points and 10 minima. Then the Morse relations were applied, which are

$$n - b + r - c = 0, \quad n \geq 1, \quad b \geq 3, \quad r \geq 3, \quad c \geq 1, \quad (4)$$

where $n$, $b$, $r$, $c$ denote the total number of nuclear, bond, ring and cage points, respectively (Morse & Cairns, 1969; Pendas *et al.*, 1997). The sets of critical points obeyed these relations and were finally checked for symmetry equivalence, yielding only seven unique critical points in the cuprite unit cell (Table 6; the maxima at Cu and O have been omitted). Results of *VALRAY* and *XD* were in good agreement.

It has to be mentioned here that several search attempts yielded more than these unique points, *e.g.*, instead of the saddle point at 0.75,0.25,0, two or three (3,+1) ring points were detected. However, a closer look always revealed that these additional points stem from incomplete refinements, *i.e.* the absolute refinement minimum was not properly found. Hence, in the following refinements, care was taken in finding the absolute minimum, *e.g.* in *VALRAY* the criterion for convergence was set to $10^{-8}$.

Some of the results of the critical point investigations are now discussed in detail.[1] The most important point in the cuprite structure is the bond critical point (3,−1) between Cu and O atoms. Tables 7 and 8 summarize the characteristics of this point derived from the various data and models. The location of the critical point varies between fractional coordinates 0.1227 and 0.1267, *i.e.* with fluctuations of about 3%. Although the differences are small, a tendency is visible. Comparing the data sets, according to the CUHE data, the bond point is closer to the copper in 0,0,0 and closer to the oxygen for the other two data sets. Comparing the models, one finds that the bond point is much closer to the copper for the EXP model.

An analogous tendency is found for the density at the critical point. The density is larger according to the CUHE data compared with the other data sets, and it is larger according to the EXP model compared with the analytical function models. However, the relative differences of these quantities are larger than the relative differences between the locations: the minimum density is 0.673 and the maximum is 0.816 e Å$^{-3}$, *i.e.* the relative difference here is about 20%.

The ratio of the principal curvatures $|\lambda_1|/\lambda_3$ and the Laplacian at a bond critical point provide information for a classification of chemical bonding. A curvature ratio $\ll 1$ is typical for closed-shell interactions, while for shared interactions the ratio increases with bond strength. Accordingly, the Laplacian is positive for a dominating closed-shell interaction and negative for covalent bonding.

Table 8 gives curvature ratios between 0.1396 and 0.1869 and Laplacians between 14.708 and 17.476 e Å$^{-5}$, respectively, both indicating an ionic dominated Cu—O bond in $Cu_2O$. The Laplacians of CUHE and CUEC are nearly identical but different from those of CULT. These findings can be well ascribed to the stronger influence of the high-order reflections on the Laplacian. CUHE and CUEC data share the same high-order reflections, while those of CULT are different. Comparing the models, the Laplacian is always larger in the refinements that used analytical function models compared with those using exponential functions.

A second bond point is found at 0.75,0.25,0 and symmetry-equivalent positions, but the charge density is very small at these critical points (Table 9). Another interesting feature of this critical point is the ellipticity, which is defined as

$$\varepsilon = (\lambda_1 - \lambda_2)/\lambda_2, \quad (5)$$

and which gives a hint for a certain amount of $\pi$ bonding in many structures. However, the ellipticity derived here is affected with large uncertainties and in some cases $\sigma(\varepsilon) > \varepsilon$, *i.e.* the values are insignificant. Hence, these findings let us assume that the charge-density modelling in this low-density region is less accurate and therefore less reliable compared with the regions closer to the nuclei and that the properties here are strongly influenced by the applied model.

[1] A complete list of all parameters of all critical points is presented at http://www-hasylab.desy.de/groups/schneider_group/ecds/ecds.html.

**Table 8**
First rows: eigenvalues $\lambda_1$ ($=\lambda_2$) and $\lambda_3$ of the Hessian; second rows: ratio $|\lambda_1|/\lambda_3$ and Laplacian $\nabla^2\rho$ (e Å$^{-5}$) at the bond critical point; source: *VALRAY*.

| Data | EXP | AN1 | AN2 | AN3 |
|---|---|---|---|---|
| CUHE | −4.106 (29) / 23.084 (36) | −4.380 (188) / 24.650 (689) | −4.412 (157) / 25.563 (760) | −4.495 (157) / 25.526 (874) |
| | 0.1779 / 14.872 (38) | 0.1777 / 15.891 (287) | 0.1726 / 16.738 (232) | 0.1761 / 16.536 (224) |
| CUEC | −4.390 (32) / 23.489 (39) | −4.284 (138) / 24.240 (631) | −4.494 (124) / 24.559 (749) | −4.521 (161) / 24.847 (792) |
| | 0.1869 / 14.708 (45) | 0.1767 / 15.673 (166) | 0.1830 / 16.323 (211) | 0.1819 / 16.282 (244) |
| CULT | −3.354 (94) / 21.993 (28) | −3.314 (185) / 23.488 (785) | −3.384 (193) / 24.244 (730) | −3.450 (190) / 24.323 (750) |
| | 0.1525 / 15.285 (173) | 0.1411 / 16.860 (260) | 0.1396 / 17.476 (296) | 0.1418 / 17.422 (275) |

**Table 9**
First rows: charge density $\rho$ (e Å$^{-3}$) and Laplacian $\nabla^2\rho$ (e Å$^{-5}$) at the second critical point; second rows: ellipticity $\varepsilon$; source: *VALRAY*.

| Data | EXP | AN1 | AN2 | AN3 |
|---|---|---|---|---|
| CUHE | 0.092† / 0.607† | 0.054 (8) / 0.700 (18) | 0.032 (1) / 0.610 (7) | 0.036 (2) / 0.661 (18) |
| | 0.031 (1) | 0.401 (280) | 0.619 (464) | 0.538 (405) |
| CUEC | 0.084 (1) / 0.510 (1) | 0.076 (2) / 0.579 (14) | 0.032 (1) / 0.613 (8) | 0.032 (2) / 0.617 (19) |
| | 0.038 (12) | 0.316 (589) | 0.335 (284) | 0.347 (314) |
| CULT | 0.094† / 0.630 (1) | 0.076 (4) / 0.599 (16) | 0.033 (1) / 0.624 (7) | 0.034 (1) / 0.647 (14) |
| | 0.175 (5) | 0.176 (278) | 0.287 (356) | 0.210 (281) |

† E.s.d. less than 0.001.

**Table 10**
Locations of the (3,+1) critical point; fractional coordinates $x$ and $y$ ($=z$); source: *VALRAY*.

| Data | EXP | AN1 | AN2 | AN3 |
|---|---|---|---|---|
| CUHE | 0.6746 (1) / 0.1548 (1) | 0.6572 (55) / 0.1364 (71) | 0.6497 (71) / 0.1209 (94) | 0.6525 (66) / 0.1260 (86) |
| CUEC | 0.6730 (1) / 0.1547 (3) | 0.6574 (71) / 0.1355 (95) | 0.6549 (61) / 0.1311 (78) | 0.6548 (65) / 0.1310 (84) |
| CULT | 0.6882 (1) / 0.1594 (2) | 0.6736 (187) / 0.1493 (217) | 0.6711 (64) / 0.1455 (82) | 0.6732 (54) / 0.1481 (69) |

The other critical points are one pale and two minima. The location of the pale varies considerably between the data sets and model types, and the coordinates are affected with large uncertainties (Table 10). One of the minima is located in the unoccupied copper tetrahedrons (*e.g.* at 0.75,0.25,0.25, Table 11). A closer look at the table reveals that here the densities derived from the different data sets do not differ very much but the densities derived from the different models differ considerably. Since the models in principle differ by the definition of the copper density functions, *i.e.* the monopoles, the quadrupoles and the hexadecapoles, again the modelling of the copper density has an important influence on the correct interpretation and the quantitative determination of the charge density in a region far from the nuclei. A strong influence of the density model on the location and properties of the critical points has also been observed in other structures. For example, Peres *et al.* (1999) used various multipole expansions in order to model the experimentally determined density of ammonium dihydrogen phosphate and they found no significant differences in the agreement factors and residual Fourier maps. On the other hand, the properties and derivatives of the bond critical points changed dramatically from model to model. Thus, in certain structures, the choice of the model, *i.e.* the basis set, is crucial for a proper evaluation and interpretation.

## 4. Space partitioning

According to the theory of topological analyses, the total charge density can be well separated into atomic basins, where the sum of the partial energies ascribed to the individual atoms is equal to the total energy (Bader & Beddall, 1972). The atomic basins can be determined by an analysis of the gradient vector field of the total charge density. Each gradient vector terminates at an attractor (normally a nucleus) and the sum of those points, from which the gradients end at the same attractor, defines an atomic basin. Thus, the basins are enclosed by surfaces, which are not crossed by gradient vectors, *i.e.* at each surface point the surface normal vector $n(\mathbf{r})$ obeys

$$\nabla\rho(\mathbf{r}) \cdot n(\mathbf{r}) = 0. \quad (6)$$

The following results are calculated using the space-partitioning algorithm included in *VALRAY*. Table 12 shows the volumes of the atomic basins, the total charge inside the copper and the oxygen basins, and the charge transfer according to these results compared with the formal charge transfer, which was calculated from the refined monopole populations. First, it is evident that in all cases the sum of the contributions from two copper basins and one oxygen basin equals the total charge of 66 electrons per asymmetric unit.

**Table 11**
Charge density $\rho$ (e Å$^{-3}$) at the (3,+3) minimum at 075,025,025; source: *VALRAY*.

| Data | EXP | AN1 | AN2 | AN3 |
|---|---|---|---|---|
| CUHE | 0.067† | 0.028 (7) | 0.013 (1) | 0.016 (2) |
| CUEC | 0.063† | 0.057 (2) | 0.013 (1) | 0.015 (1) |
| CULT | 0.072† | 0.057 (20) | 0.014 (2) | 0.016 (1) |

† E.s.d. less than 0.001.

**Table 12**
First rows: total charge from integration of the densities inside the atomic basins (Cu and O); second rows: calculated charge transfer from Cu towards O from space partitioning and from monopole populations; third rows: atomic volumes of Cu and O basins (Å$^{-3}$); source: *VALRAY*.

| Data | EXP | AN1 | AN2 | AN3 |
|---|---|---|---|---|
| CUHE | 28.16 / 9.68 | 28.53 / 8.94 | 28.50 / 9.00 | 28.54 / 8.92 |
| | 0.84 / 0.59 | 0.47 / 0.43 | 0.50 / 0.58 | 0.46 / 0.55 |
| | 13.67 / 11.58 | 14.20 / 10.52 | 13.71 / 11.48 | 13.69 / 11.53 |
| CUEC | 28.43 / 9.14 | 28.54 / 8.88 | 28.69 / 8.62 | 28.71 / 8.58 |
| | 0.57 / 0.34 | 0.46 / 0.24 | 0.31 / 0.37 | 0.29 / 0.36 |
| | 13.74 / 11.43 | 13.96 / 11.00 | 13.94 / 11.02 | 13.94 / 11.02 |
| CULT | 28.30 / 9.40 | 28.46 / 9.08 | 28.67 / 8.65 | 28.71 / 8.59 |
| | 0.70 / 0.48 | 0.54 / 0.31 | 0.33 / 0.39 | 0.29 / 0.37 |
| | 13.61 / 11.59 | 13.83 / 11.14 | 13.88 / 11.04 | 13.86 / 11.09 |

This can be regarded as an indication that the space-partitioning algorithm worked quite well with the high-energy synchrotron data. Second, it is also obvious that, according to all results, the charge transfer is far from 1 electron, but in most cases in the regime of 0.4 to 0.6 electrons, which is close to chemical considerations (Wang & Schwarz, 2000). Third, the charge transfer derived from the space partitioning in most cases is larger than that from the simple comparison of the monopoles, a fact that has already been observed for other structures (Kirfel, 2000). Since the atomic basins are covering the whole space in the cell, which is evident from the volumes given in Table 12, we assume that the partitioning of the density far from the nuclei is responsible for these differences.

A comparison of the results using the various charge-density models, however, yields rather different results. For the CUHE data, the charge transfer is always about 0.5 electrons, both from the monopole populations and from the space partitioning. Only in the case of the partitioning from CUHE–EXP (*i.e.* using data set CUHE and model EXP) is the transfer significantly larger.

The CUEC data yields an approximately 0.1–0.2 electrons lower charge transfer. Here, only the partitioning values of CUEC–EXP and CUEC–AN1 are in the 0.5 electrons regime. The CULT data values show rather large variations between 0.29 and 0.7 electrons.

Comparison of the models shows that the values based on the analytical function refinements are lower than those of EXP. An explanation might be given with respect to the population of the valence monopoles. In the analytical function models, the outer monopole of the copper atom is occupied with 19 (AN1), 18 (AN2) and 10 (AN3) electrons, respectively (omitting the charge transfer). The valence monopoles in the EXP model, however, are only populated with the charge, which was transfered from Cu to O (−CT for copper and +2CT for oxygen). Thus, the EXP model is more flexible for modelling the density in the interatomic regions. This assumption is underlined by the smaller aggreement indices (Table 4).

**Table 13**
Component $\nabla E_{zz}$ of the electric field gradient at the copper site in units of $10^{22}$ V m$^{-2}$; source: *VALRAY*.

| Data | EXP | AN1 | AN2 | AN3 |
|---|---|---|---|---|
| CUHE | 2.511 | 6.286 | 5.431 | 5.563 |
| CUEC | 5.833 | 5.645 | 5.742 | 5.981 |
| CULT | 2.009 | 2.039 | 2.220 | 2.196 |

## 5. Electric field gradient

An interesting feature of the cuprite structure is the considerably large component of the electric field gradient (EFG) tensor at the copper site along [111] ($\nabla E_{zz}$). Krüger & Meyer-Berkhout (1952) and Kushida *et al.* (1956) reported $|\nabla E_{zz}| = 1.34 \times 10^{22}$ and $1.02 \times 10^{22}$ V m$^{-2}$, respectively, measured by nuclear quadrupole resonance. These results were numerically supported by an evaluation of 22 keV synchrotron data by Kirfel & Eichhorn (1990). Using direct-space calculations according to Stewart (1979), the refinements yielded $\nabla E_{zz} = 1.04 - 1.44 \times 10^{22}$ V m$^{-2}$, *i.e.* always positive signs.

Theoretical calculations of the EFG, however, yielded quite different results. According to cluster calculations of Nagel (1985), the sign is negative, whereas an ionic point-charge model (Hafner & Nagel, 1983) leads to a positive sign. Recent calculations of Petrilli *et al.* (1998) using the linear augmented plane-wave and the projector augmented wave methods yielded $-0.83$ and $-0.86 \times 10^{22}$ V m$^{-2}$, respectively.

The results of our refinements are obtained by direct-space calculations using *VALRAY* and are shown in Table 13. The sign of $\nabla E_{zz}$ is always positive, but the numerical values are slightly larger compared with those of Kirfel & Eichhorn (1990). The best agreement was found for the low-temperature data. Unfortunately, the error calculation of the EFG is not yet implemented in *VALRAY* and so we estimated the uncertainty by calculating various EFG's using variations of the multipole parameters according to their standard uncertainties. The relative standard uncertainties of the EFGs were found to be 20–30% (depending on the model), *i.e.* even small deviations in the parameters yielded considerable changes of $\nabla E_{zz}$.

Deformation features close to the nuclei and with very important contributions to $\nabla E$ make it difficult to determine the EFG from X-ray measurements with sufficient accuracy (Lecomte, 2000). This would explain the quantitative differences between our results and those of earlier measurements

by Kirfel & Eichhorn (1990). However, the accuracy should be good enough to underline the positive sign of $\nabla E_{zz}$.

## 6. Electrostatic potential

In order to extend the analysis of the data, some other properties were calculated. Fig. 3 shows the electrostatic potential in the Cu—O plane, derived from EXP densities. The potential $\Phi$ due to a charge-density distribution $\rho$ centred at a nucleus $M$ with charge $Z_M$ is defined as

$$\Phi(r') = \sum_M \frac{Z_M}{R_M - r'} - \int \frac{\rho(r)}{|r - r'|}\,\mathrm{d}r, \qquad (7)$$

and is therefore a long-range property. Thus, for simplicity, the maps in Fig. 3 are calculated assuming only a Cu—O—Cu—O—Cu partial structure, which allows qualitative comparisons of the potential near the nuclei, whereas the quantitative values are somewhat arbitrary. The potential maps in Figs. 3(*a*), (*c*) and (*e*) indicate no significant differences between the data sets and no hint of any charge localization between the atoms, *i.e.* no covalent bonding was found. In order to study differences between the data sets, additional potential distributions were calculated neglecting the non-spherical multipoles. These distributions were subtracted from the total potentials, and finally maps were calculated according to these 'deformation potentials'. The deformation part of CUHE and CUEC data (Figs. 3*b* and *d*) is mainly dominated by the quadrupoles at the Cu site, whereas only marginal structures are visible near the O nuclei. The CULT data, however, also show some 'deformation potential' near oxygen. It has to be mentioned that the scale of these maps is approximately three orders of magnitude less than that of Figs. 3(*a*), (*c*) and (*e*), which explains the similarity of the 'total potential' maps.

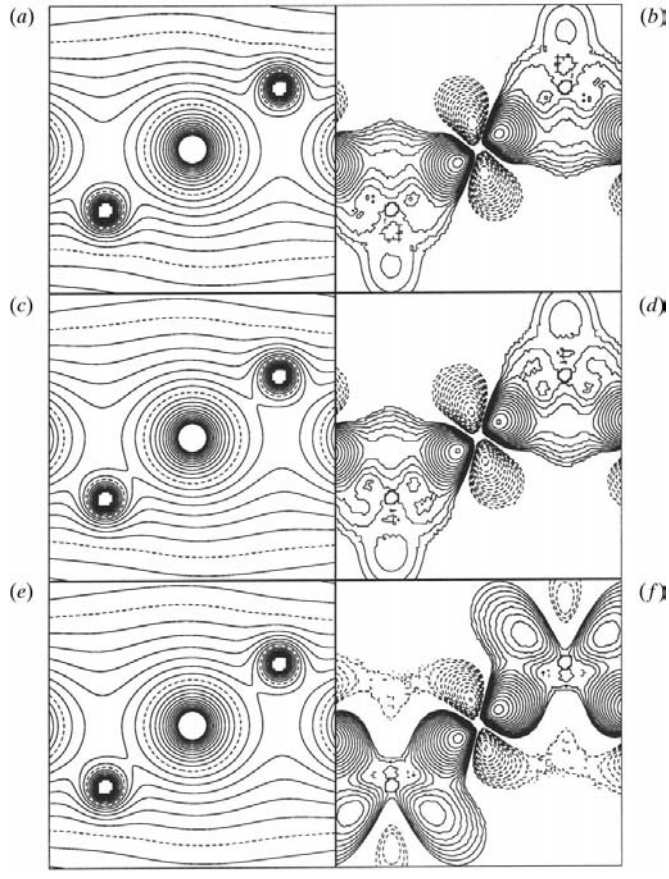


**Figure 3**
Potential maps in the (110) plane calculated from (*a*) CUHE–EXP, (*c*) CUEC–EXP and (*e*) CULT–EXP, and corresponding 'deformation potential' maps (*b*), (*d*) and (*f*) (explanation in the text). Source: *XD*.

## 7. Laplacian of the charge density

The values of the Laplacian distribution, which is defined as

$$L(r) = -(\hbar^2/4m)\nabla^2\rho(r), \qquad (8)$$

at the critical points are presented in Tables 6, 8 and 9. The Laplacian relief maps calculated from the three data sets using

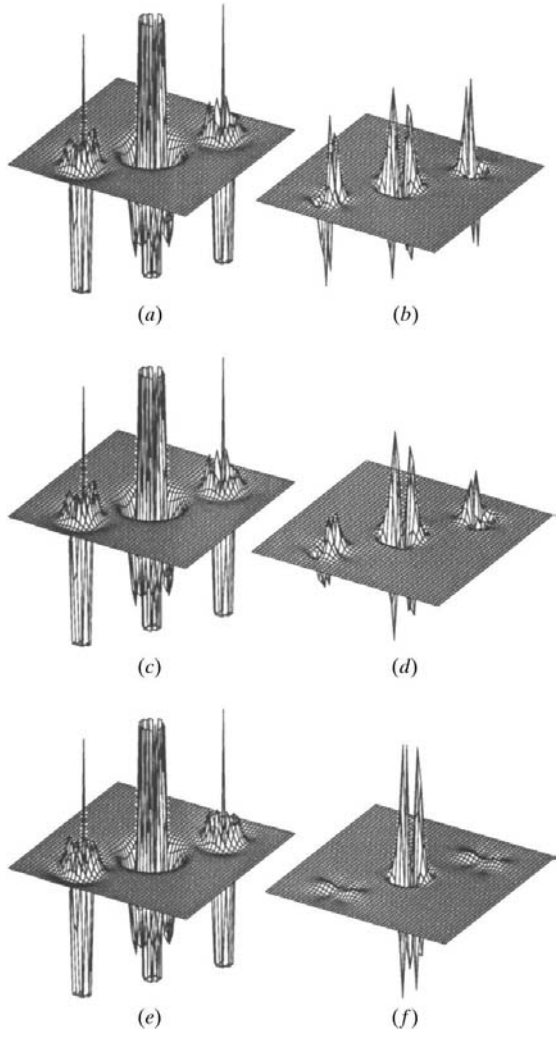


**Figure 4**
Laplacian relief maps in the (110) plane calculated from (*a*) CUHE–EXP, (*c*) CUEC–EXP and (*e*) CULT–EXP and corresponding 'deformation Laplacian' maps (*b*), (*d*) and (*f*) (explanation also in the text). Source: *XD*.

model EXP, as an example, are also rather similar, both near the nuclei and in the interatomic regions (Figs. 4*a*, *c* and *e*). In particular, there are no spikes or features along the bond paths and the atoms are well separated, which is again an indication of the ionic bonding in the cuprite structure. Differences are only visible in the 'deformation Laplacian', which is calculated in the same manner as the 'deformation potential' presented above. Here, the most pronounced features result from CUHE, while the spikes near oxygen are considerably lower in the CUEC map and nearly invisible for CULT.

## 8. Density on the 'empty' tetrahedral sites

Recently, some discussions took place about the presence of a charge-density accumulation on the 'empty' tetrahedral sites in the cuprite structure (Fig. 5). Zuo *et al.* (1999) published results from an analysis of combined electron diffraction and X-ray data, where they found a local density maximum of 0.2 e Å$^{-3}$ in the interstitial regions, from which they concluded that a significant amount of covalent bonding between the copper atoms exists.

According to quantum-chemical calculations using density-functional methods and self-consistent perturbation theory (SCF–MP2), Wang & Schwarz (2000) reported no maxima on these sites and a density below 0.08 e Å$^{-3}$. This value is in agreement with our results. As an example, Fig. 6 shows the densities derived using CUHE–EXP. For example, the total density at the site 0.75,0.25,0.25 is 0.067 e Å$^{-3}$ and $\sigma(\rho)$ is 0.00505 e Å$^{-3}$.

The residual density ($\rho_o - \rho_c$) in Figs. 6(*e*) and (*f*) yields $\sim -0.12$ e Å$^{-3}$ on the site, *i.e.* according to the measured structure factors there is even less density in the tetrahedra than derived from the refined model. According to Table 11, all refinements yielded densities between 0.013 and 0.072 e Å$^{-3}$, *i.e.*, even if there is a large uncertainty about the quantitative value, our data provide no hints for a charge accumulation inside the tetrahedra.

Since the copper sublattice is face-centred cubic, it could easily be compared with the lattice of pure copper but the cardinal difference between these lattices is the copper–copper distance, which is 2.556 Å in copper and 3.019 Å in cuprite. Wang & Schwarz (2000), however, pointed out that the attractors in cuprite may have their origins in the superposition of the tails of copper *d*–*s* hybrids and that interactions are only possible up to distances of about 2.5 Å at maximum. Since, according to the chemical considerations, the Cu—Cu distance in cuprite is too large for an interaction of the ions, the (3, −1) bond point that we found here (Table 9) could also be an artefact of the superposition of the *d*–*s* hybrid tails mentioned above (Schwarz, 2000).

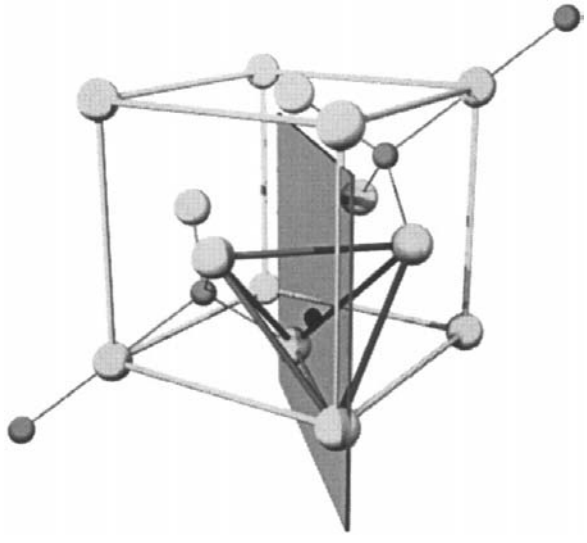

**Figure 5**
Structure of cuprite. Large light spheres: Cu; small darker spheres: O. A unit cell is indicated by the light sticks, and one of the tetrahedra by the dark sticks, respectively. Additionally, the plane investigated in Fig. 6 is shown and the centre of the tetrahedron is indicated as a black dot.

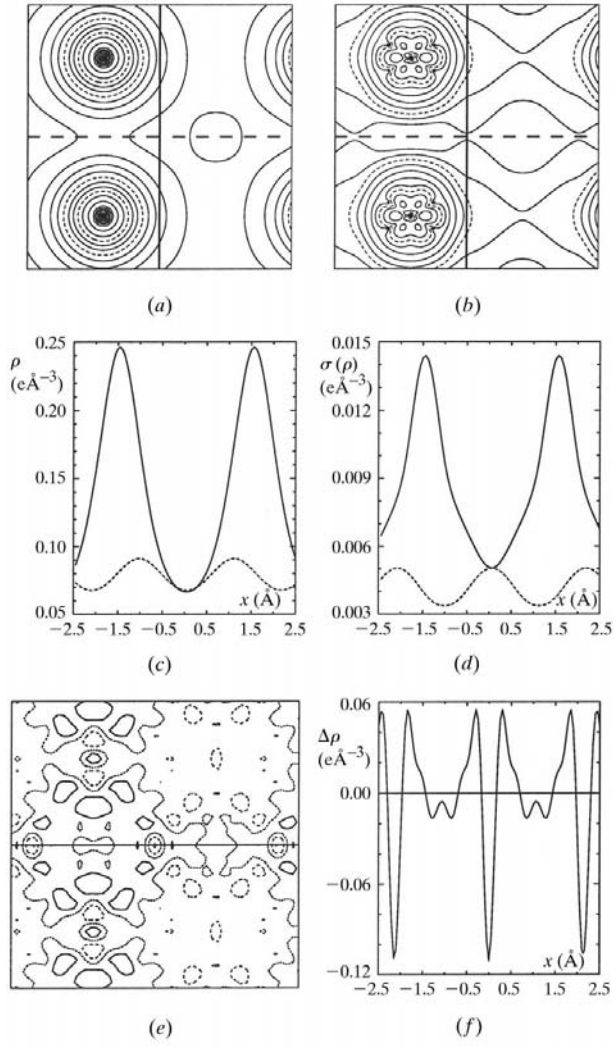


**Figure 6**
(*a*) Charge density in a plane including the tetrahedral interstitial void at 0.75,0.25,0.25 in the centre. Contour lines as in Fig. 1. Horizontal axis: [001], vertical axis: [$\bar{1}$10]. (*b*) Corresponding error map. The density and error along the horizontal (broken) and vertical lines (solid) are shown in (*c*) and (*d*). The residual density along the horizontal line in (*e*) is presented in (*f*). Source: *VALRAY*.

## 9. Conclusions and summary

The results of our investigation of the charge density of cuprite have shown that high-energy synchrotron data are well suited for reliable topological analyses and the derivation of further properties from the charge-density distribution. Moreover, the comparison of our data sets and the comparison of the different models provides detailed experimental insight on the copper–oxygen bonding in cuprite and can thus help to answer open questions.

The various refinements show both similarities and differences. With respect to the analyses of the bond critical points and the space partitioning, we can confirm that the bonding in the cuprite structure is dominated by ionic interactions. The charge transfer derived from both monopole populations and space partitioning was found in the range ~0.4–0.6 electrons in most cases, which is consistent with chemical considerations. The principal curvatures, the Laplacians and the electrostatic potentials at the Cu—O bond critical point also give evidence for an ionic bonding scheme in $Cu_2O$. Further similarities found in all analyses are the existence of only seven unique critical points (Table 6), however, the densities at the non-bonding points are small and can differ considerably depending on both the model and the data set considered.

When the different data sets are compared, it is not possible to prefer or reject one of our measurements. In most cases, the marginal differences can be ascribed to the different composition of the data sets, *i.e.* number and type of weak reflections. When the different models are compared, however, significant differences between the EXP model on the one hand and the AN models on the other hand were found in almost all investigations, which can mainly be ascribed to the kind of copper monopole functions used. Conclusively, if results of refinements of different structures have to be compared, it is essential to use the same model functions in the refinements.

A comparison of the results from the programs *VALRAY* and *XD* was not discussed in detail, mainly because of the good agreement between the refinements and the results of the topological analyses with both programs, if the refinement start values were properly chosen. Thus, all presented results can be well ascribed to the data, the models and the structure.

We thank R. F. Stewart, Carnegie–Mellon University for providing the analytical functions of $Cu^+$, and A. Kirfel, University of Bonn, and W. H. E. Schwarz, University of Siegen, for fruitful discussions. Many thanks to C. Flensburg, University of Copenhagen, for help with *VALRAY* and Th. Richter, TU Berlin, for help with *XD*.

## References

Abramov, Y. A. (1997). *Acta Cryst.* A**53**, 264–272.
Bader, R. F. W. (1990). *Atoms in Molecules: a Quantum Theory.* Oxford: Clarendon Press.
Bader, R. F. W. & Beddall, P. M. (1972). *J. Chem. Phys.* **56**, 3320.
Bouchard, R., Hupfeld, D., Lippmann, T., Neuefeind, J., Neumann, H.-B., Poulsen, H. F., Rütt, U., Schmidt, T., Schneider, J. R., Süssenbach, J. & von Zimmermann, M. (1997). *J. Synchrotron Rad.* **5**, 90–101.
Clementi, E. & Roetti, C. (1974). *At. Data Nucl. Data Tables*, **14**, 177.
Cruickshank, D. W. J. & Robertson, A. P. (1953). *Acta Cryst.* **6**, 698.
Espinosa, E., Molins, E. & Lecomte, C. (1998). *Chem. Phys. Lett.* **285**, 170–173.
Flaig, R., Koritsanszky, T., Zobel, D. & Luger, P. (1998). *J. Am. Chem. Soc.* **120**, 2227–2238.
Flensburg, C., Larsen, S. & Stewart, R. F. (1995). *J. Phys. Chem.* **99**, 10130–10141.
Gatti, C., Bianchi, R., Destro, R. & Merati, F. (1992). *J. Mol. Struct. (Theochem.)*, **255**, 409–433.
Hafner, S. & Nagel, S. (1983). *Phys. Chem. Miner.* **9**, 19–22.
Humphreys, C. J. (1999). *Nature (London)*, **401**, 21–22.
Irle, S., Lin, H. L., Niu, J. E. & Schwarz, W. H. E. (1992). *Ber. Bunsenges. Phys. Chem.* **96**, 1545–1551.
Johnson, C. K. & Burnett, M. (1996). *Crystallographic Topology and its Applications in Crystallographic Computing*, edited by P. E. Bourne & K. Watenpaugh. Seattle: Western Washington University/Chester: IUCr.
Kirfel, A. (2000). Private communication.
Kirfel, A. & Eichhorn, K. (1990). *Acta Cryst.* A**46**, 271–284.
Koritsanszky, T., Howard, S., Richter, T., Su, Z., Mallinson, P. R. & Hansen, N. K. (1995). *XD. Computer Program Package for Multipole Refinement and Analysis of Electron Densities from X-ray Diffraction Data.* Freie Universität Berlin, Berlin, Germany.
Krüger, H. & Meyer-Berkhout, U. (1952). *Z. Phys.* **132**, 171–178.
Kushida, T., Benedek, G. B. & Bloembergen, N. (1956). *Phys. Rev.* **104**, 1364.
Lecomte, C. (2000). Private communication.
Lewis, J., Schwarzenbach, D. & Flack, H. D. (1982). *Acta Cryst.* A**38**, 733–739.
Lippmann, T. & Schneider, J. R. (2000). *J. Appl. Cryst.* **33**, 156–167.
Marksteiner, P., Blaha, P. & Schwarz, K. (1986). *Z. Phys.* B**64**, 119–127.
Morse, M. & Cairns, S. S. (1969). *Critical Point Theory in Global Analysis and Differential Geometry.* New York: Academic Press.
Nagel, S. (1985). *J. Chem. Phys. Solids*, **46**, 743–756.
Pendas, A. M., Costales, A. & Luana, V. (1997). *Phys. Rev. B*, **55**, 4275–4284.
Peres, N., Boukhris, A., Souhassou, M., Gavoille, G. & Lecomte, C. (1999). *Acta Cryst.* A**55**, 1038–1048.
Petrilli, H. M., Blöchl, P. E., Blaha, P. & Schwarz, K. (1998). *Phys. Rev. B*, **57**, 14690–14697.
Politzer, P. & Truhlar, D. G. (1981). Editors. *Chemical Applications of Atomic and Molecular Electrostatic Potentials.* New York/London: Plenum Press.
Restori, R. & Schwarzenbach, D. (1986). *Acta Cryst.* B**42**, 201–208.
Schwarz, W. H. E. (2000). Private communication.
Schwarz, W. H. E., Mensching, L., Ruedenberg, K., Valtazanos, P., Miller, L. L., Jacobson, R. & von Niessen, W. (1989). *Angew. Chem. Int. Ed. Engl.* **28**, 597–600.
Schwarz, W. H. E., Mensching, L., Valtazanos, P. & von Niessen, W. (1986). *Int. J. Quantum Chem.* **30**, 439–444.
Souhassou, M. & Blessing, R. H. (1999). *J. Appl. Cryst.* **32**, 210–217.
Spackman, M. A. (1992). *Chem. Rev.* **92**, 1769–1797.
Stewart, R. F. (1979). *Chem. Phys. Lett.* **65**, 335–342.
Stewart, R. F. (1999). Private communication.
Stewart, R. F. & Spackman, M. A. (1983). *VALRAY Users Manual*, Edition 1. Department of Chemistry, Carnegie–Mellon University, Pittsburgh, PA 15213, USA.
Wang, S. G. & Schwarz, W. H. E. (2000). *Angew. Chem. Int. Ed. Engl.* Submitted.
Zuo, J. M., Kim, M., O'Keeffe, M. & Spence, J. C. H. (1999). *Nature (London)*, **401**, 49–52.